



Synthesis and coherent properties of ^{13}C -enriched sub-micron diamond particles with nitrogen vacancy color centers

Yuliya Mindarava^a, Rémi Blinder^a, Yan Liu^a, Jochen Scheuer^{a,g}, Johannes Lang^a, Viatcheslav Agafonov^b, Valery A. Davydov^c, Christian Laube^d, Wolfgang Knolle^d, Bernd Abel^d, Boris Naydenov^{e,*}, Fedor Jelezko^{a,f}

^a Institute for Quantum Optics, Ulm University, Ulm, 89081, Germany

^b GREMAN, UMR CNRS-7347, Université F. Rabelais, Tours, 37200, France

^c L.F. Vereshchagin Institute for High Pressure Physics, RAS, Troitsk, Moscow, 142190, Russia

^d Department of Functional Surfaces, Leibniz Institute of Surface Engineering, Leipzig, 04318, Germany

^e Institute for Nanospectroscopy, Helmholtz-Zentrum Berlin für Materialien und Energie GmbH, Berlin, 14109, Germany

^f Centre for Integrated Quantum Science and Technology (IQST), Ulm, 89081, Germany

^g NVision Imaging Technologies GmbH, Ulm 89081, Germany

ARTICLE INFO

Article history:

Received 12 October 2019

Received in revised form

2 March 2020

Accepted 22 April 2020

Available online 30 April 2020

Keywords:

Dynamic nuclear polarization

HPHT diamond growth

^{13}C isotopic enrichment

P1 center

NV^- center

ABSTRACT

Here we report the synthesis of ^{13}C -enriched diamond powder with sub-micron particle sizes via High Pressure High Temperature (HPHT) growth. Diamond powder with a tailored isotopic enrichment is particularly interesting for implementation of Dynamic Nuclear spin Polarization (DNP) and ^{13}C enrichment plays an important role for increasing the signal to noise ratio in Nuclear Magnetic Resonance (NMR) and Magnetic Resonance Imaging. We applied Electron Paramagnetic Resonance (EPR) and NMR spectroscopy to the sub-micron diamond material as well as Optically Detected Magnetic Resonance (ODMR) and atomic force microscopy to investigate preselected nano-sized particles. The ^{13}C spin concentrations were evaluated with NMR for the initial particle ensemble and with ODMR for the nanodiamond fraction, showing the homogeneous distribution of ^{13}C density in particles with different sizes. The ^{13}C nuclear spin-lattice relaxation decay (T_1) shows a multiexponential behavior, where the fast relaxing component is attributed to relaxation from surface defects. Additionally, an optical method for estimating the NV^- concentration in nanodiamonds is presented. The obtained powder is promising as a base material for the production of ^{13}C -enriched nanodiamonds for DNP applications.

© 2020 The Authors. Published by Elsevier Ltd. This is an open access article under the CC BY license (<http://creativecommons.org/licenses/by/4.0/>).

1. Introduction

Magnetic resonance imaging (MRI) is a widely used technique and a common tool for medical diagnostic and for monitoring anatomical and physiological processes in living organisms. However, it often suffers from low sensitivity, preventing early diagnosis of certain diseases, especially tumors, mainly due to the low polarization of nuclear spins at ambient conditions. Dynamic nuclear spin polarization (DNP) is a well established method for transferring the few orders of magnitude higher electron spin polarization to nuclear spins [1–4]. Recently combined DNP-MRI experiments have been realized in patients, where a tumor could be

imaged only when hyperpolarized MRI agents were used [5].

Using negatively-charged Nitrogen-Vacancy (NV^-) color centers in diamond as a system for implementing DNP and MRI is of interest due to several reasons [6]. First, the electron spin associated with NV^- can be polarized above 92% at room temperature by laser illumination [7]. Second, diamonds can be shrunk to nanoscale-sized crystals (nanodiamonds), and it has been demonstrated that functionalized nanodiamonds (NDs) are non-toxic and biocompatible [8–10], making them attractive nano-probes for non-invasive long term applications in life sciences. Last but not least, the long relaxation time of ^{13}C nuclear spins $^{\text{C}13}\text{T}_1$ in diamond [11] would allow to implement DNP protocols [12–17] and to realize hyperpolarized NDs for MRI applications.

Increasing the ^{13}C content above natural abundance (1.109%) is a promising route to increase the hyperpolarization potential. Performing DNP on a ^{13}C -enriched diamond was already reported to

* Corresponding author.

E-mail address: boris.naydenov@helmholtz-berlin.de (B. Naydenov).

lead to a stronger hyperpolarized signal [18]. Additionally, the high density of magnetic nuclei is expected to allow distributing the polarization through the lattice at a higher spin diffusion rate [19,20]. Combining this benefit with the high surface-to-volume ratio of nanodiamonds could provide the opportunity to polarize external spins in liquid by transferring the polarization outside the diamond crystal [21–23]. Fabrication of diamond powder with both high ^{13}C and NV^- concentration, together with surface functionalization, is seen as a route towards opening novel opportunities for high contrast MRI, e.g. in pre-clinical imaging, that would rely on the real-time monitoring and tracking of ND particles inside of living animals [24]. Here, we report the synthesis and characterization of submicron diamond particles with tailored isotopic composition, as a step towards the production of nanodiamonds with a controlled ^{13}C content for DNP applications.

2. Results and discussion

2.1. Synthesis

Commercially available nanodiamonds are produced by milling down bulk diamond crystals [25] or micro-size crystals [26,27]. The drawback of this material for biological applications is its toxicity, due to the sharp edges created during the milling process [28]. In contrast, High Pressure High Temperature (HPHT) diamond powder has the advantage of a much smoother surface providing higher biocompatibility and reduced concentration of surface defects [8,29].

The earlier diamond synthesis techniques at high pressures and high temperatures were implemented by using different mixtures of graphite and graphite-like materials in the presence of metal catalysts [30]. The novelty of our approach for HPHT diamond synthesis consists in using a pure hydrocarbon growth system without adding any metal catalyst [31]. By using additional organic and heteroorganic compounds in the growth system, one can obtain various types of doped diamond particles, including diamond particles with optically active impurities (SiV, GeV, etc.) [32,33], or with a controlled degree of ^{13}C enrichment.

The HPHT synthesis of the ^{13}C -enriched diamond powder was realized in a hydrocarbon metal catalyst-free growth system, using homogeneous mixtures of naphthalene C_{10}H_8 (Chemapol), which plays the role of the main source of carbon and hydrogen in the growth system, detonation ultrananosized (3–5 nm) diamonds C_{ND} (SkySpring Nanomaterials, 0510HZ) with natural abundance of ^{13}C isotope, and benzoic acid $^{13}\text{C}_6\text{H}_5\text{COOH}$ (Cambridge Isotope Laboratories), where the latter was used as the “ ^{13}C -doping” component. The mass ratio can be found in Table 1. The samples investigated in this article are labeled according to their isotopic content: naC13 for the sample with natural abundance of ^{13}C , 5C13, 14C13, 20C13 and 30C13 for the samples with respectively 5%, 14%, 20% and 30% ^{13}C enrichment. The ^{13}C content was determined for all samples through NMR (see NMR subsection). The 20C13 samples originate from two different synthesis batches, and are therefore labeled accordingly, 20C13-1 and 20C13-2.

The obtained samples have been first characterized by scanning electron microscopy (SEM). Fig. 1a shows a typical SEM image of the 20C13-2 sample before irradiation. We observe exclusively diamond particles, which points to a high yield of diamond material formation. The histogram in Fig. 1b shows the particle size distribution extracted from several SEM pictures (similar to Fig. 1a). We observe a broad size distribution ranging from 50 nm to about 2 μm .

Although a wide distribution of sizes exists, one can select particles with an appropriate size depending on the specific application requirements. While nanodiamonds of small size would be preferable for bioapplications, microdiamonds might have

better spin properties (comparable to those of bulk diamond). For the optical measurements (subsections “Atomic Force Microscopy (AFM) and Confocal Microscopy” and “Optically Detected Magnetic Resonance (ODMR)”) we have preselected only nanosized particles (50–170 nm) (see Experimental section).

Electron irradiation and annealing were performed on the 20%-enriched samples. This method allows to convert substitutional nitrogens in diamond (P1 centers) into NV^- [34,35]. The process goes as follows: (1) high-energy electron irradiation creates vacancies in the lattice, and (2) annealing at high temperature (usually 800 °C) makes the vacancies mobile, which allows (after diffusion in the crystal) their trapping by P1 centers to form NV^- centers. While these two steps are usually performed in a successive fashion [34,35], high temperature (800 °C) irradiation was performed on the 20C13-1 sample, i.e. simultaneous irradiation and annealing were performed. The motivation behind using this method [36] is the expected reduced formation of undesirable divacancies [37] and vacancy clusters [38]. These defects are competitive to the formation of NV^- and additionally induce spin decoherence [39]. Due to the instantaneous mobilization of the single formed vacancies, a permanent low concentration of vacancies is realized that hinders the formation of divacancies/vacancy clusters. In contrast, the sample 20C13-2 was irradiated at room temperature, and subsequently annealed (800 °C). To indicate in tables and figures the data that is relevant to the irradiated samples, we add ‘(ir)’ at the end of the sample label.

2.1.1. Electronic paramagnetic resonance (EPR)

The most common defect in diamond is the substitutional nitrogen atom (P1) center [40,41], which is paramagnetic with an electron spin $S = 1/2$. As the creation of NV^- centers ($S = 1$) relies on the trapping of irradiation-induced vacancies by P1 centers, the NV^- concentration after irradiation depends on the initial P1 concentration, where a high concentration of the latter shortens the relaxation and coherence times of ^{13}C nuclear spins in the diamond lattice, as well as the coherence time of the NV^- electron spins [42].

Therefore, determination of the P1 concentration is an essential aspect of the characterization of diamond powder in the prospect of DNP applications. The results obtained for the concentration, spin-lattice relaxation (1T_1) and coherence (1T_2) times of P1 centers are presented in Table 2.

In this work, two methods have been used to determine the P1 concentration: the absolute spin quantification, using continuous wave (CW) EPR and the analysis of instantaneous diffusion (ID) with pulsed EPR (see Supporting Information). The spin-counting with CW EPR is a direct measure of an extrinsic quantity, the absolute number of spins in the full sample. In contrast, instantaneous diffusion gives measure of an intrinsic quantity, i.e. the average distance between two adjacent electron spins [43–45]. The advantage of ID is that, it can be used for concentration determination without using a spin standard. The results presented in Table 2 show that both methods give consistent values. The fact that datasets from both techniques are in good agreement,

Table 1

Respective quantities of precursors used in the growth system (mass fraction, with respect to naphthalene).

Sample	^{13}C conc.	Naphthalene	DND	Benzoic acid
name	(%)	C_{10}H_8		$^{13}\text{C}_6\text{H}_5\text{COOH}$
naC13	1.11	1	2	–
5C13	5±0.5	1	2	0.3
14C13	14±1.5	1	2	0.65
20C13	20±2	1	2	0.7
30C13	30±3	1	2	1

indicates that there is a homogeneous distribution of P1 centers in the sample.

In order to understand the sources of P1 decoherence and relaxation, we measured the spin-lattice relaxation (${}^{\text{P1}}T_1$) and coherence (${}^{\text{P1}}T_2$) times for the different samples. Three main decoherence mechanisms for P1 centers are expected - spectral diffusion caused by dipolar interaction with other paramagnetic defects, flip-flop processes in the nuclear spin bath and ID [46,47]. The latter is a modulation of the dipolar interaction among the probed species resulting from spin-flips induced by the refocusing π -pulse [48]. This mechanism can be quantified by measuring Hahn echo decays for different rotation angles of the second microwave pulse, which can be done, e.g., by adjusting the pulse length t_p (see Supporting Information, Fig. 4a).

To quantify the contribution to decoherence from mechanisms other than instantaneous diffusion, we consider the value of T_2 in the limit $t_p \rightarrow 0$ [46], which we label $T_{2,\text{noID}}$ (see Supporting Information, Equation (2)). This value decreases with increasing P1 concentration. A possible reason is that ${}^{\text{P1}}T_2$ is reduced by spectral

diffusion caused by random flip-flops of P1 centers, and therefore also depends on their concentration [42].

The values for NV^- concentration estimated with spin-counting in CW EPR are presented in Table 3. As the NV^- spectrum is highly anisotropic, only a part of it was integrated in order to estimate the NV^- concentration. To estimate the total amount of spins the obtained number of spins was multiplied by a factor (ratio between the integrated part of the spectrum and full spectrum) taken from the simulated NV^- spectrum. The obtained result for the high temperature irradiated sample demonstrates a higher conversion efficiency from P1 to NV^- .

The effect of instantaneous diffusion on the T_2 time of NV^- centers can be neglected as the concentration of NV^- centers is much lower than the one of P1 centers. This could explain why instantaneous diffusion could not be observed for NV^- centers, meaning that the main mechanism for NV^- decoherence is spectral diffusion.

The T_2 and T_1 times of NV^- centers in the sample 20C13-2 are 1.2 μs and 2.2 ms, respectively. In spite of high concentration of P1 spins and ${}^{13}\text{C}$ nuclear spins in the diamond lattice, the results demonstrate long coherence of the spin system.

The EPR spectrum of NV^- in diamond powder is highly anisotropic and the spectral shape is described by a Pake doublet [49], with two intensive lines for NV^- whose crystal axis is oriented perpendicular to the magnetic field [50]. The electron spin echo (ESE) EPR spectrum of NV^- was measured with and without light excitation on the irradiated 20C13-2 sample. As shown in Fig. 2, an enhancement of NV^- polarization under laser illumination, which is a prerequisite for hyperpolarization, has been observed. To account for the interaction of the center with light, a simulation was performed by considering an enhanced population in the $m_S = 0$ spin state of the NV^- (see Supporting Information, subsection "Simulation of the optically polarized NV^- spectrum"). As shown in Fig. 2, the most important features seen in the experimental spectrum - in particular in the region of the intensive lines at 2900 G and 3900 G - are well reproduced by the simulation. As the efficiency of optical polarization of NV^- depends on the alignment between magnetic field and crystal axis of the center, the enhancement of the signal is inhomogeneous and dominates for the spins which are either perpendicular or parallel to the magnetic field [51]. The determined enhancement of the intensive line close to 2900 G (perpendicular NVs) when illuminating with 100 mW laser power is approximately 6-fold.

2.2. Nuclear Magnetic Resonance (NMR)

The NMR measurements were performed at room temperature, in an external magnetic field $B = 7.05\text{T}$. On the NMR spectra shown in Fig. 3, the y-axis intensity was normalized to the mass of the sample. For the ${}^{13}\text{C}$ -enriched samples, this allows for estimation of the degree of enrichment: the concentration of ${}^{13}\text{C}$ spins was determined by integration over the mass-normalized ${}^{13}\text{C}$ NMR spectrum (Fig. 3) and by comparison of the integral with

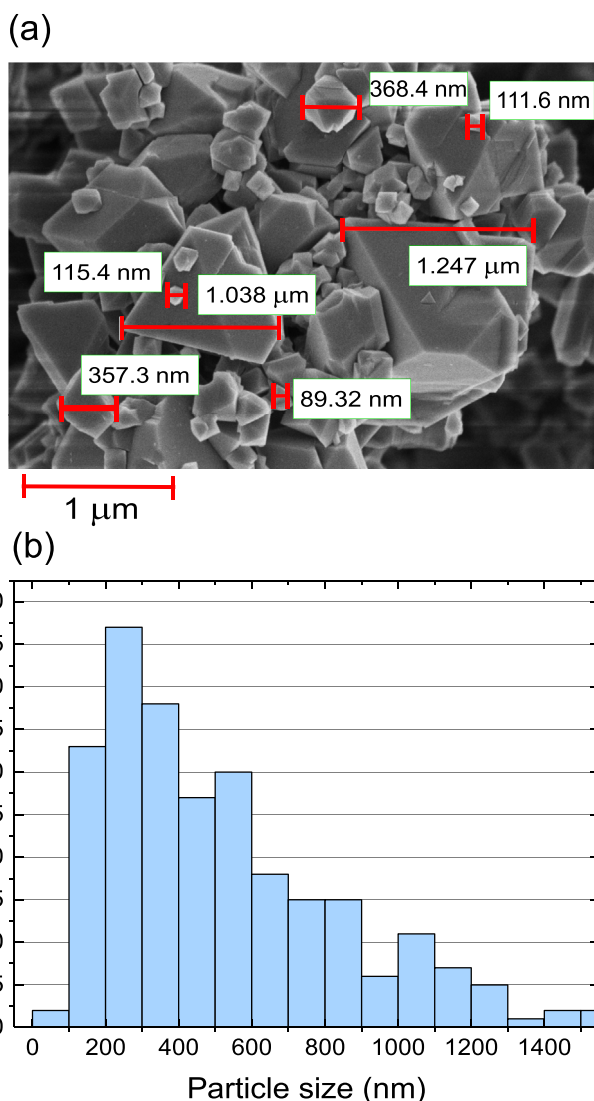


Fig. 1. (a) SEM image of the 20% ${}^{13}\text{C}$ -enriched sample 20C13-2 taken after chemical and ultrasonic treatment and before electron irradiation. (b) Histogram showing the particle size distribution obtained by analyzing several SEM images. (A colour version of this figure can be viewed online.)

Table 2

Electron spin properties of P1 centers in the sub-micron diamond samples, see text for more details.

Sample name	P1 conc., CW (ppm)	P1 conc., ID (ppm)	${}^{\text{P1}}T_2$ in absence of ID (μs)	Hahn-echo ${}^{\text{P1}}T_2$ (μs)	${}^{\text{P1}}T_1$ (ms)
naC13	74	73	1.46	0.42	1.7
5C13	116	92	0.84	0.48	0.8
14C13	177	141	0.40	0.24	0.5
20C13-1	139	167	0.70	0.31	0.7
30C13	92	93	1.22	0.82	1.4

measurements on powder with natural ^{13}C abundance (and comparable P1 concentrations).

We remark that the full width at half maximum (FWHM) of the ^{13}C spectral line is increasing with ^{13}C content, which reveals that internuclear ^{13}C – ^{13}C couplings play a role in the broadening. Up to 20% enrichment, the lineshape was fitted with a Lorentzian function, while the 30% spectrum was fitted with a Voigt function (the fit parameters are given in Supporting Information, section NMR Measurements). We model the evolution of the FWHM linewidth (shown in the inset of Fig. 3) as:

$$\Delta_{\text{FWHM}} = \sqrt{w_{\text{off}}^2 + (w_{\text{dd}}n_{13\text{C}})^2} \quad (1)$$

This expression accounts for contributions from two independent broadening processes: a background process (w_{off} term), that originates from the paramagnetic lattice defects, and, a process that originates from the ^{13}C dipole-dipole coupling. For low concentrations of magnetic nuclei, dipole-dipole coupling is indeed expected to yield a linear increase of the FWHM with the concentration ($n_{13\text{C}}$), hence the second term $w_{\text{dd}}n_{13\text{C}}$ [52,53]. Fitting the FWHM data for all samples yields $w_{\text{off}} = 1.20$ KHz and $w_{\text{dd}} = 14.8$ KHz. At high concentrations of magnetic nuclei, the lineshape is expected to develop Gaussian features [52], which probably explains the Voigt (combination of Gaussian and Lorentzian) shape of the 30% spectrum.

An important parameter related to DNP applications is the nuclear spin-lattice relaxation time, T_1 . As shown in Fig. 4, the saturation-recovery measurements of T_1 reveal for all samples a biexponential recovery. The values obtained for fitted parameters are summarized in Table 4. It should be noted here that the biexponential decay is just an approximation for a more complex relaxation process, e.g. multiexponential distribution of relaxation times. The fact that such a distribution is observed reveals an inhomogeneity in the system (for a homogeneous system with randomly distributed paramagnetic centers, one expects rather a “stretched exponential” recovery [54]).

We attribute the observed distribution to two types of hyperfine interaction of ^{13}C nuclear spins - to paramagnetic defects at the diamond surface (unpaired electrons) and to paramagnetic defects deeper (<100 nm) in the diamond crystal (mainly P1 centers). The former lead to a fast relaxation (described by T_{1s}), while the latter show slow relaxation (T_{1l}) [11,55]. The fraction of ^{13}C sensitive to surface relaxation depends on the particle size distribution (illustrated on Fig. 1b for the 20C13-2 sample). All samples described in the present study contain dominantly particles in the submicron range - although the exact size distribution may vary slightly from one sample to another.

To focus on the overall rate of relaxation, we consider the characteristic time ($T_{1,1/e}$) when the nuclear magnetization ($M(t)$) has reached up to a fraction $(1 - 1/e) \approx 63\%$ of the fully recovered value. The variation of $T_{1,1/e}$ across samples, shown in Table 4, is not trivial, and likely results from the interplay between different parameters (^{13}C and P1 concentration, size distribution). We would like to discuss it here.

Table 3
The P1 and NV^- concentrations in irradiated samples.

Sample name	Irradiation	P1 conc., CW (ppm)	P1 conc., ID (ppm)	NV^- conc. CW (ppm)
20C13-1(ir)	high temp. irr.	81	108	10
20C13-2(ir)	room temp. irr.	37	32	2

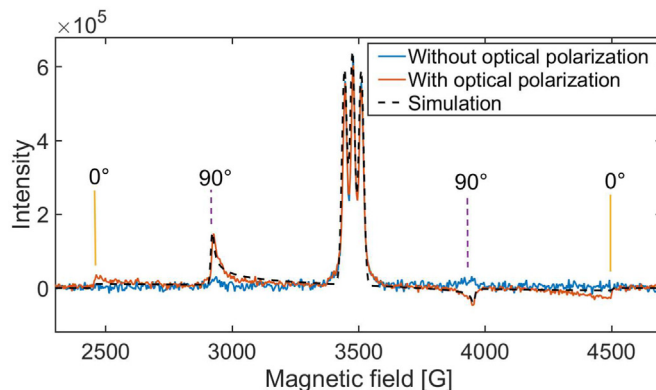


Fig. 2. ESE-EPR spectrum of the 20% ^{13}C -enriched sample (20C13-2), both in the dark and under 532 nm light illumination (at 100 mW laser power), showing both the P1 centers (three central peaks) and NV^- (broader component spreading between 2400 and 4500 G). The vertical lines illustrate the positions of spectral lines corresponding to certain NV^- orientations with respect to magnetic field (purple dashed for 90° and solid yellow for 0°). Simulation of the spectrum under illumination was performed by considering the additional light-induced polarization of NV^- in the $m_s = 0$ spin state (see text). (A colour version of this figure can be viewed online.)

The effect of increasing the ^{13}C content can be inferred by comparing the data available for both natural abundance and 30% ^{13}C -enriched sample (for which the P1 concentrations are close - 74 and 92 ppm respectively). With 30% ^{13}C enrichment, we observe a sharp decrease of $T_{1,1/e}$, which is a factor of 10 lower in comparison to its natural abundance counterpart. We attribute this important decrease to the enhanced spin diffusion coefficient as a result of stronger internuclear nearest-neighbour couplings in the ^{13}C -enriched sample [56,57].

Considering the data for the 20C13-1 sample, one can also try to describe how the irradiation process affects the T_1 relaxation. For this sample $T_{1,1/e}$ increases from 5.0 s to 9.1 s with irradiation (Table 4). This effect can originate from the decrease in the overall concentration of bulk paramagnetic defects (P1 and NV^-) after irradiation. Indeed, the creation of each NV^- is accompanied by the creation of one non-magnetic N^+ , so the total concentration of paramagnetic defects must decrease. The concentrations of P1 and NV^- reported in Tables 2 and 3 support this hypothesis (see discussion in Supporting Information, section “Effect of irradiation on P1 and NV^- concentrations”). Comparing the samples irradiated with the two techniques, we observe that sample 20C13-2(ir) shows a slower relaxation rate compared to sample 20C13-1(ir). As P1 is significantly lower in the sample that has slow relaxation (37 ppm), one can assume that the change in the speed of relaxation originates from the difference in P1 concentration.

However, we should remark that the above-mentioned hypotheses are not systematically followed, which points to variations in the contribution from surface relaxation. In particular sample 20C13-1(ir) and 30C13 have comparable concentration of P1 centers (81 and 92 ppm, respectively), but we observe a longer $T_{1,1/e}$ in the 30C13 sample, despite the higher ^{13}C density. Slightly different particle size distributions for the two samples may explain this effect. Smaller grain size in the 20C13-1(ir) sample may lead to a more important fraction of ^{13}C within a certain distance from the surface, for which T_1 is shortened due to relaxation from surface defects.

Further work (for instance, measuring separately different size fractions) would help in quantifying the respective roles of the different relaxation mechanisms. Such work should also benefit the understanding of the effect of ^{13}C content.

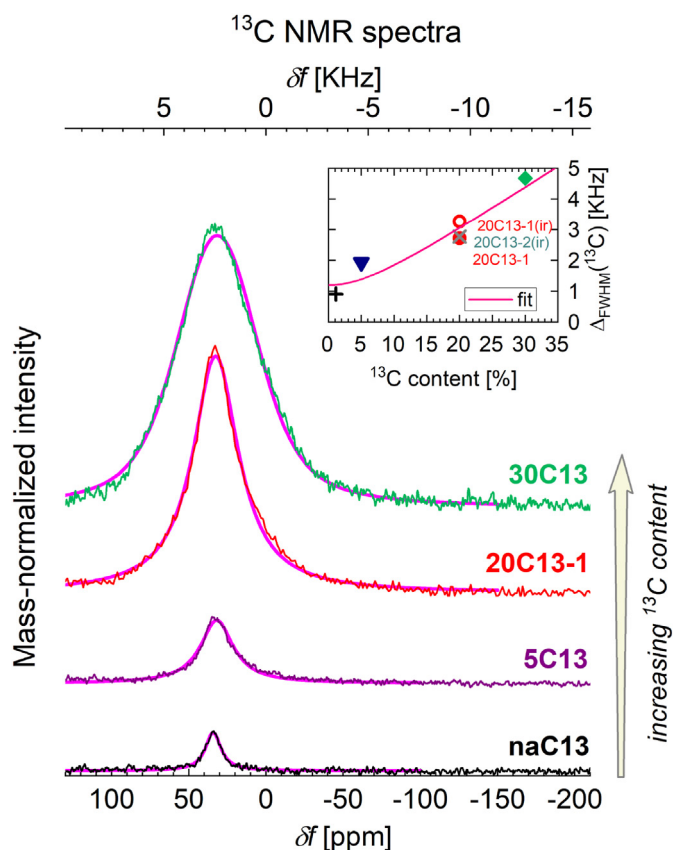


Fig. 3. Mass-normalized ^{13}C NMR spectra of the submicron powder (non-irradiated). The magenta lines correspond to fits of the spectra using a Lorentzian or Voigt function, see text. Inset: Full Width at Half Maximum (FWHM) of the NMR line (including the irradiated samples), and fit with Eq. (1). (A colour version of this figure can be viewed online.)

2.3. Atomic force microscopy (AFM) and confocal microscopy

With a combined confocal microscope and atomic force microscope (AFM) setup, both size and fluorescence properties of a single nanodiamond can be studied simultaneously (Fig. 5). Since the resolution in the xy plane is limited by the spatial extent of the cantilever tip, the height of nanodiamond particles h was used to estimate their size. It was determined as the lateral distance between the highest point and the surface level of the substrate.

The number of NV^- centers in one ND can be estimated (assuming all the ND orientations fluoresce equally) as $N_{\text{NV}} = \frac{I_{\text{ND}}}{I_{\text{NV}}}$, where I_{ND} is the fluorescence intensity of the ND and I_{NV} is the fluorescence intensity of a single NV^- center. I_{NV} is determined on a ND sample which has single NV^- centers, using the same laser power ($50\mu\text{W}$) as for the measurements in this study. Fig. 6 shows the measured N_{NV} for different particles as a function of their height h . To describe this data, we first model the ND volume as $V = C_{\text{sh}}h^3$, where C_{sh} is a proportionality factor which depends on the ND average shape. Then the number of NV^- in one given ND reads:

$$N_{\text{NV}} = A[\text{NV}]V = A[\text{NV}]C_{\text{sh}}h^3 = ah^3, \quad (2)$$

where $[\text{NV}]$ is the NV^- density in units of parts per million (ppm), $A = \rho \frac{10^{-6}N_A}{M}$, ρ is the density of the diamond, N_A is the Avogadro constant and M is the atomic mass of carbon.

From Equation (2), the NV^- concentration reads $[\text{NV}] = \frac{a}{C_{\text{sh}}A}$. The a parameter was determined from fitting the experimental data

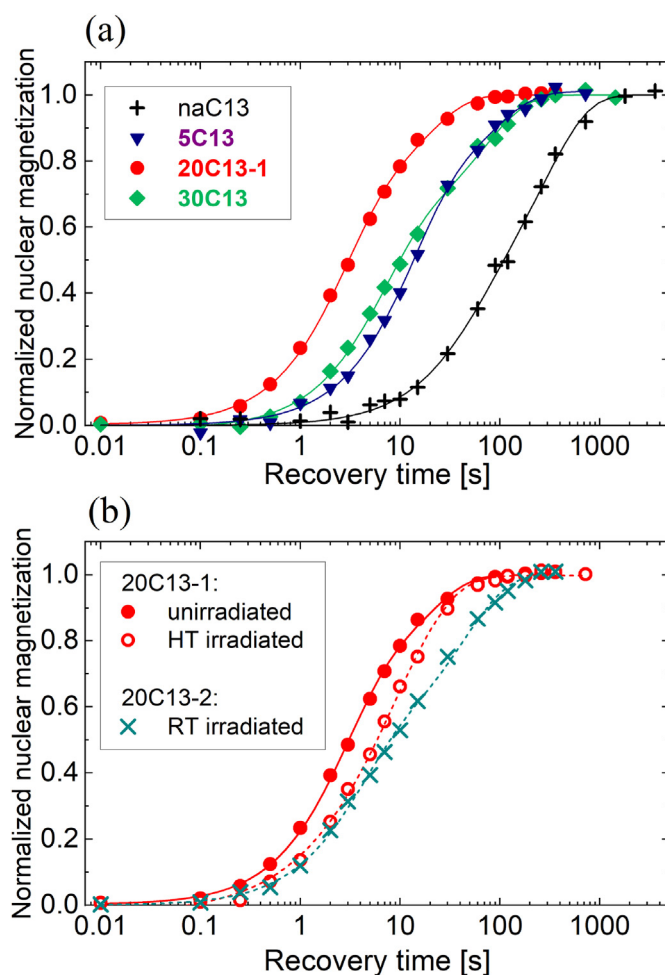


Fig. 4. Saturation-recovery measurements, revealing the ^{13}C nuclear spin relaxation times for: (a) the samples with different ^{13}C content, before irradiation and (b) the samples with 20% ^{13}C enrichment, both before and after irradiation. The intensity is normalized to the fully recovered magnetization ($t \rightarrow \infty$) obtained from the fit. (A colour version of this figure can be viewed online.)

Table 4

^{13}C spin-lattice relaxation parameters for all samples. The parameter ${}^{13}\text{C}T_{1,1/e}$, corresponds to the time at $(1 - 1/e) \approx 63\%$ recovery (see text). After fitting the recovery with a biexponential function, $M(t)/M_{\infty} = 1 - a_s \exp(-t/T_{1s}) - (1 - a_s) \exp(-t/T_{1l})$, we obtained the parameters T_{1s} , T_{1l} (fitted short and long relaxation times) and a_s (fitted weight of the short relaxation component).

Sample	^{13}C conc. (%)	P1 conc., (ppm)	${}^{13}\text{C}T_{1,1/e}$ (s)	${}^{13}\text{C}T_{1s}$ (s)	${}^{13}\text{C}T_{1l}$ (s)	a_s	fit R^2
naC13	1.11	74	186.3	44.4	289.0	0.31	0.997
5C13	5 ± 0.5	116	22.0	12.7	83.2	0.68	0.998
14C13	14 ± 1.5	177	3.5	1.9	12.2	0.65	0.999
20C13-1	20 ± 2	139	5.0	2.7	17.9	0.65	0.999
20C13-1(ir)	20 ± 2	81	9.1	3.5	18.4	0.46	0.999
20C13-2(ir)	20 ± 2	37	16.9	3.7	44.3	0.47	0.999
30C13	30 ± 3	92	18.5	6.5	69.2	0.57	0.999

(Fig. 6). Although the shape of nanodiamonds is predominately octahedral, some variation exists, which causes an uncertainty on C_{sh} , and therefore on NV^- density. To account for this variability, we assume the shape of nanodiamonds to be distributed between octahedral and spherical (see Supporting Information, section “Importance of the ND shape in the NV^- spin counting”), which

yields $[NV] = 0.4 \pm 0.1$ ppm.

We identified two potential reasons for the value of NV^- concentration to be estimated lower than with EPR. The first one being the smaller average size of the optically investigated nanodiamonds (see Experimental Section). Their larger surface to volume ratio increases the relative size of the region in which NV^- centers can not be created [58]. The second being that a fluorescence based method suffers from blinking and bleaching of NVs during the measurement. Therefore one might on average detect a lower amount of NV^- centers in contrast to EPR, where all NV^- centers are detectable.

2.4. Optically detected magnetic resonance (ODMR)

The spin of single or multiple nitrogen vacancy centers in nanodiamonds can be measured using optically detected magnetic resonance (ODMR) in a confocal microscopy setup. Here, we present results related to the 20C13-2 sample demonstrating how, as a complement to the NMR measurement, determination of the ^{13}C concentration can be achieved through the measurement of ODMR spectra from NV^- ensembles in single ND.

Presence of ^{13}C atoms in the first shell of NV^- center leads to a distinct 127 MHz splitting of the central line, due to the strong hyperfine interaction [59]. Here we neglect the hyperfine interaction with the ^{14}N nuclear spin (2.2 MHz), which is small compared to the hyperfine interaction associated with a first neighbour ^{13}C . Expressed in the frame of the NV^- center, the hyperfine Hamiltonian has its z-axis along the NV^- symmetry axis, the x-axis in the symmetry plane and the y-axis perpendicular to both. The Hamiltonian describes the interaction between electron spin of the NV^- center ($S = 1$) and ^{13}C atom ($I = 1/2$) in the first shell and takes the following form:

$$H_{hf} = A_{zz}S_zI_z + A_{xx}S_xI_x + A_{yy}S_yI_y + A_{xz}(S_xI_z + S_zI_x), \quad (3)$$

where S_i I_i are the electron and nuclear spin operators and A_{lm} are the components of the hyperfine tensor. The complete Hamiltonian of NV^- center and ^{13}C can then be written as:

$$H = DS_z^2 + \gamma_e BS + \gamma_n BI + H_{hf}, \quad (4)$$

where $D = 2.87$ GHz is the zero-field splitting of the electron spin, B is the magnetic field, γ_e and γ_n are the gyromagnetic ratios of the electron and nuclear spins respectively and $\gamma_e BS$ is the electron spin Zeeman term.

The degree of ^{13}C enrichment determines the ODMR spectrum. There is an additional splitting of about 25 MHz associated with an external magnetic field B_0 of approximately 9G. ^{13}C abundance in the diamond can be estimated by the line splitting in the ODMR spectrum associated with the coupling of NV^- centers to ^{13}C atoms

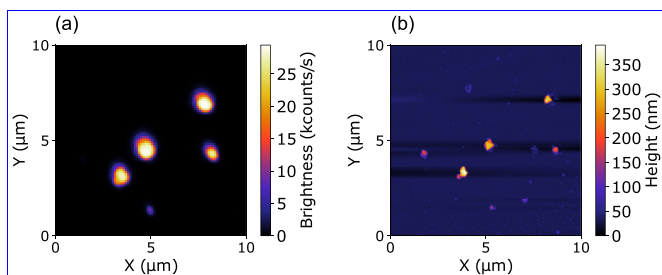


Fig. 5. Fluorescence image (a) and topography image (b) of single ND crystals from an AFM aligned with a confocal microscope. (A colour version of this figure can be viewed online.)

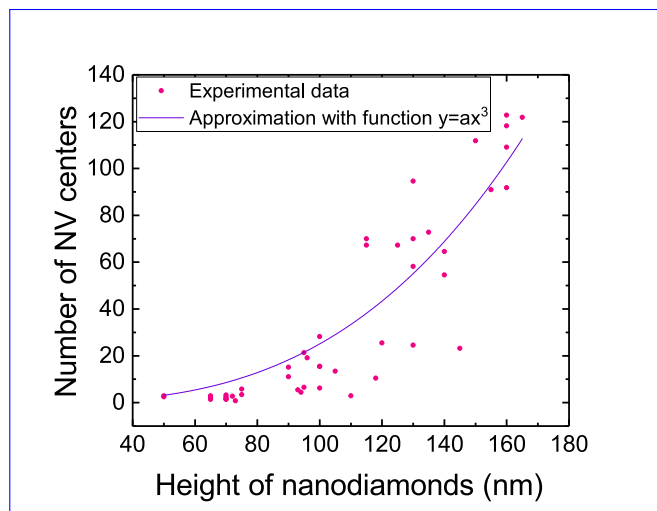


Fig. 6. The estimation of NV^- density with the confocal-AFM setup using 50 nanodiamond particles and fitted with the function $y = ax^3$. The resulting NV^- concentration is 0.4 ± 0.1 ppm. (A colour version of this figure can be viewed online.)

in their vicinity, as $x = \frac{1}{3b+c}$, where c and b correspond to the contrast of ODMR dips in the case, respectively, of one ^{13}C in the first NV^- shell and no ^{13}C in the first NV^- shell. The cases of two or three ^{13}C atoms in the first shell have been neglected since they show low ODMR contrast.

The ODMR spectra of nanodiamonds are fit with a function which consists of six Gaussians yielding the respective values for ^{13}C concentration, see Fig. 7. The average ^{13}C enrichment determined by measuring ODMR spectra on 20 different nanodiamond particles is $18.7 \pm 1.5\%$, which is consistent with the value obtained by standard NMR on the same sample, see Table 4. In comparison with quantitative NMR, the method for estimation of ^{13}C concentration based on acquiring ODMR requires a much smaller amount of nanodiamonds and can be used when only small sample quantity is available. With above-mentioned methods the ^{13}C enrichment can be quantified and a concentration value can be assigned to a set of fabrication parameters.

2.5. Discussion

Although the particle size distribution in the produced powder is broad, ranging from 50 nm to 2 μm , comparison of the NMR data (relevant to the full ensemble of particles) and ODMR (relevant only to the nanodiamond fraction, i.e. <200 nm) demonstrate the ^{13}C enrichment is homogeneous across particles with different sizes.

The future perspective for HPHT growth would be to develop a technique which allows to control the P1 concentration during the synthesis. This would not only be beneficial for DNP, but also applications where good spin properties are required. In the prospect of DNP applications, an important target for improving the HPHT growth would be to achieve the synthesis of nanodiamonds with a narrower size distribution through a control of the growth conditions, and ultimately to increase the production yield of diamond nano-crystals with desired size.

Practically, the ability to perform hyperpolarization experiments is closely related to the T_1 time of the ^{13}C nuclear spins. If one wants to polarize an external solution, a long T_1 is an asset. Indeed, the polarization can only be transferred to the solution from bulk defects that are located within the “spin-diffusion length” from the surface, which scales as $L \propto \sqrt{DT_1}$ (where D is the coefficient of spin-diffusion between the bulk ^{13}C) [18], longer T_1 would lead to more

polarization channels towards the external solution being available. Alternatively, if nanodiamonds are to be used as MRI contrast agents, T_1 is also an important parameter as it dictates the final ^{13}C polarization level. Indeed, as the time during which nuclear polarization builds up in DNP is limited by T_1 [60], the latter therefore controls the detected NMR signal. Additionally, in biomedical MRI, the relaxation time has to be long enough to allow performing the steps needed before image acquisition (e.g., injection of the product into the subject and diffusion through the body) [61].

The envisioned DNP applications with nanodiamonds, such as contrast agent for MRI, require much smaller ND sizes ($<50\text{ nm}$). Our results (section 2.2) show that the relaxation rate has contribution both from bulk paramagnetic defects and surface impurities. We recognize that for particles with sizes of less than 50 nm , surface effects are naturally expected to be stronger. Therefore, it is to be expected that producing nanodiamonds for DNP applications would require optimizing the surface properties to eliminate or neutralize relaxing species on the surface. We look forward to the continuation of promising progress that has recently been reported in that direction [62].

3. Conclusions

We demonstrate here the fabrication using HPHT technique of submicron diamond powder with quasi-spherical shaped particles having both high NV^- concentration and ^{13}C isotopic enrichment. The latter can be tuned by selecting the ^{13}C content in the initial carbon material used for the synthesis and quantified with NMR or ODMR spectroscopy. The ^{13}C enrichment was found to be homogeneous across the particles with different sizes. The analysis of ^{13}C spin-lattice relaxation reveals a multiexponential recovery, where we attribute the fast component to surface-induced relaxation and the slow component to bulk paramagnetic defects, which are dominantly P1 centers. As a fraction of the formed particles consists

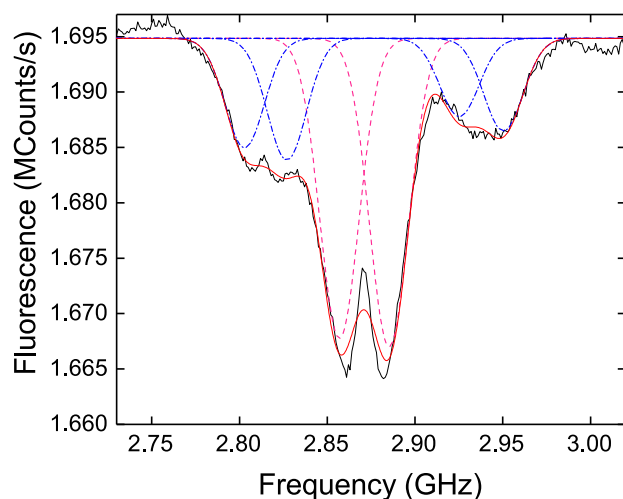


Fig. 7. Example of a fit for the ODMR spectrum (black full line) of a NV^- ensemble in ND consisting of 6 superposed Gaussian functions. We only take NV^- centers with one ^{13}C atom in the first shell (blue dash-dotted line) and without any ^{13}C atoms (pink dashed line) into account. The different intensities are probably related to the mixing between the electron and nuclear spin states, leading to different strengths of the EPR transitions. The full simulated spectrum (red full line) comprises the spectra of both NV^- groups and the overall concentration of ^{13}C atoms can be estimated from their relative weight. This spectrum was obtained by performing the summation on datasets acquired separately on 20 nanodiamond grains. The average ^{13}C concentration is $(18.7 \pm 1.5)\%$. (A colour version of this figure can be viewed online.)

in nanodiamonds (size $< 200\text{ nm}$), the obtained diamond powder could constitute a base material for the production of ^{13}C -enriched nanodiamond samples.

4. Experimental Section

4.1. HPHT crystal growth

The synthesis of diamonds with different ^{13}C content was performed in a high-pressure apparatus of the “Toroid” type using homogeneous mixtures of naphthalene C_{10}H_8 , C_{ND} nanodiamonds, and isotopically-enriched benzoic acid $^{13}\text{C}_6\text{H}_5\text{COOH}$. Cylindrical samples of this material (5mm diameter and 3mm height), obtained by cold pressing, were inserted into graphite containers, which also served as heaters. The experimental procedure consisted in loading the apparatus up to 8GPa, heating it up to 1500°C and a short isothermal exposure under constant load for 5–10s. Afterwards the obtained diamond products are isolated by quenching to room temperature under pressure [63,64]. The removal of non-diamond products of transformation was carried out by chemical treatment of the samples in highly concentrated acid mixture (HNO_3 , HClO_4 and H_2SO_4) at 200°C for 5 h. Ultrasonic dispersion of the diamond particles in water or alcohol was performed using the Hielscher UP200Ht dispersant.

4.2. Irradiation and annealing

The samples were irradiated using two different methods. For the first one the 20C13-2 sample was irradiated with $2 \times 10^{18}\text{ cm}^{-2}$ irradiation dose in a 10 MeV electron accelerator (MB10-30 MP-Mevex Corp., Stittsville Canada) at air atmosphere under permanent cooling to regulate the treatment temperature below 300°C . After irradiation the samples were additionally annealed in argon atmosphere at 800°C for 5 h. Surface graphite formed during this treatment was removed via oxidation in air at 620°C for 5 h. A more detailed description of the approach can be found in Laube et al. [35]. For the second approach (high temperature irradiation) the sample 20C13-1 was irradiated within a ceramic holder placed in a quartz furnace under permanent argon flow and with irradiation dose to be $2 \times 10^{18}\text{ cm}^{-2}$. The treatment temperature was regulated by the dose per pulse and repetition frequency of the accelerator. The temperature was monitored applying a thermo-element connected to the sample holder. The temperature was regulated to be 800°C . Surface graphite formed during this treatment was removed via oxidation at air at 620°C for 5 h.

4.3. EPR

X-band (9.6 GHz) CW and Pulse EPR measurements were implemented at room temperature on a Bruker Elexsys E580 EPR spectrometer with waveguide (ER-4122MD4) and FlexLine (ER-4118X-MD5) resonators. For spin-counting in CW we used the Bruker software (xEPR). For optical spin polarization of the NV^- center a laser (LRS-0532 DPSS) with wavelength 532 nm and a fiber (M93 L02 Thorlabs with $1500\mu\text{m}$ diameter and $\text{NA} = 0.39$) have been used. Simulations of EPR spectra were performed using the EasySpin Matlab toolbox [65].

4.4. NMR

NMR experiments were performed using a 300 MHz WB system at a magnetic field of field $B = 7.05\text{ T}$, in combination with an Avance III console, both from Bruker Biospin GmbH. The corresponding Larmor frequency of ^{13}C at this field is $f(^{13}\text{C}) = 75.513\text{ MHz}$.

4.5. Fluorescence imaging and sample preparation

For optical and AFM investigation only a fraction of small diamond crystals with a size of less than 200 nm was prepared. This was done by dissolving sample 20C13-2 in demineralized water and sonicating it in a Branson 3510 ultrasonic cleaning bath to disaggregate ND clusters. Then, the solution with diamond powder was kept in a fixed vertical position for weeks to allow larger diamond particles to precipitate and smaller diamonds were selected by pipetting the upper part of the sample liquid. The glass substrate was plasma cleaned to minimize background fluorescence. For sample preparation 5 μ L of solution was spin-coated on the glass substrate at 5000 rpm for 40 s. Microwaves were applied on NV⁻ centers through a copper wire. Fluorescence and optically detected magnetic resonance (ODMR) spectra were measured with a home-built confocal microscope. For the excitation of NV⁻ centers a solid-state laser with a wavelength of 532 nm was used and focused onto the sample using an oil-immersion objective (Olympus UPlanSApo 60x oil NA = 1.35). Fluorescence was filtered by a bandpass filter (Transmission window: from 625.5 nm to 795.2 nm) and then detected by an avalanche photodiode with single photon resolution (Excelitas Technologies). The size of the diamond particles has been detected with an atomic force microscope setup from JPK Instruments.

Declaration of competing interest

The authors declare that they have no known competing financial interests or personal relationships that could have appeared to influence the work reported in this paper.

CRediT authorship contribution statement

Yuliya Mindarava: Formal analysis, Investigation, Validation, Writing - original draft, Writing - review & editing, Visualization. **Rémi Blinder:** Methodology, Formal analysis, Investigation, Validation, Writing - original draft, Writing - review & editing, Visualization. **Yan Liu:** Formal analysis, Investigation, Visualization, Writing - original draft. **Jochen Scheuer:** Formal analysis, Investigation, Validation, Writing - original draft. **Johannes Lang:** Investigation. **Viatcheslav Agafonov:** Investigation, Resources. **Valery A. Davydov:** Investigation, Resources. **Christian Laube:** Investigation, Resources. **Wolfgang Knolle:** Investigation, Resources. **Bernd Abel:** Investigation, Resources, Supervision, Funding acquisition. **Boris Naydenov:** Conceptualization, Methodology, Writing - original draft, Writing - review & editing, Investigation, Supervision. **Fedor Jelezko:** Conceptualization, Methodology, Resources, Supervision, Funding acquisition.

Acknowledgements

This work was supported by the DFG (CRC 1279), EU HYPERDIAMOND (Project ID 667192), VW Stiftung (No. 93432), BW Stiftung (No. BWINTSFIII-042), BMBF (Project No. 13N14438, 13GW0281C, 13N14808, 16KIS0832, 13N14810, 13N14990), ERC (Grant No. 319130). V.A.D. thanks the Russian Foundation for Basic Research (Grant No. 18-03-00936) for financial support.

We thank Prof. Isoya, Dr. Eichhorn and Dr. Genov for fruitful discussions on the acquisition and analysis of EPR data.

Appendix A. Supplementary data

Supplementary data to this article can be found online at <https://doi.org/10.1016/j.carbon.2020.04.071>.

References

- [1] E. Ravera, C. Luchinat, G. Pari, J. Magn. Reson. 264 (2016) 78–87.
- [2] E.C. Reynhardt, G.L. High, J. Chem. Phys. 109 (1998) 4100–4107.
- [3] A. Henstra, W. Wenckebach, Mol. Phys. 112 (2014) 1761–1772.
- [4] J. Wolber, F. Ellner, B. Fridlund, A. Gram, H. Jóhannesson, G. Hansson, L. Hansson, M. Lerche, S. Månsson, R. Servin, M. Thaning, K. Golman, J. Ardenkjær-Larsen, Nucl. Instrum. Methods Phys. Res., Sect. A 526 (2004) 173–181.
- [5] S.J. Nelson, J. Kurhanewicz, D.B. Vigneron, P.E.Z. Larson, A.L. Harzstark, M. Ferrone, M. van Criekinge, J.W. Chang, R. Bok, I. Park, et al., Sci. Transl. Med. 5 (2013).
- [6] M.W. Doherty, N.B. Manson, P. Delaney, F. Jelezko, J. Wrachtrup, L.C.L. Hollenberg, Phys. Rep. 528 (2013) 1–45.
- [7] G. Waldherr, J. Beck, M. Steiner, P. Neumann, A. Gali, T. Frauenheim, F. Jelezko, J. Wrachtrup, Phys. Rev. Lett. 106 (2011) 157601.
- [8] V. Vajjayanthimala, H.-C. Chang, Nanomedicine 4 (2009) 47–55.
- [9] K.-K. Liu, C.-L. Cheng, C.-C. Chang, J.-I. Chao, Nanotechnology 18 (2007) 325102.
- [10] Y. Zhu, J. Li, W. Li, Y. Zhang, X. Yang, N. Chen, Y. Sun, Y. Zhao, C. Fan, Q. Huang, Theranostics 2 (2012) 302.
- [11] E.C. Reynhardt, G.L. High, Prog. Nucl. Magn. Reson. Spectrosc. 38 (2001) 37–81.
- [12] D. Pagliero, K.R.K. Rao, P.R. Zangara, S. Dhomkar, H.H. Wong, A. Abril, N. Aslam, A. Parker, J. King, C.E. Avalos, A. Ajoy, J. Wrachtrup, A. Pines, C.A. Meriles, Phys. Rev. B 97 (2018), 024422.
- [13] I. Schwartz, J. Scheuer, B. Tratzmiller, S. Müller, Q. Chen, I. Dhand, Z.-Y. Wang, C. Müller, B. Naydenov, F. Jelezko, M.B. Plenio, Sci. Adv. 4 (2018) 8978.
- [14] Q. Chen, I. Schwarz, F. Jelezko, A. Retzker, M.B. Plenio, Phys. Rev. B 92 (2015) 184420.
- [15] P. London, J. Scheuer, J.-M. Cai, I. Schwarz, A. Retzker, M.B. Plenio, M. Katagiri, T. Teraji, S. Koizumi, J. Isoya, R. Fischer, L.P. McGuinness, B. Naydenov, F. Jelezko, Phys. Rev. Lett. 111 (2013), 067601.
- [16] R. Wunderlich, J. Kohlrautz, B. Abel, J. Haase, J. Meijer, J. Phys. Condens. Matter 30 (2018) 305803.
- [17] R. Wunderlich, J. Kohlrautz, B. Abel, J. Haase, J. Meijer, Phys. Rev. B 96 (2017) 220407.
- [18] A.J. Parker, K. Jeong, C.E. Avalos, B.J.M. Hausmann, C.C. Vassiliou, A. Pines, J.P. King, Phys. Rev. B 100 (2019), 041203.
- [19] G.R. Khutsishvili, Phys. Usp. 8 (1966) 743–769.
- [20] A. Ajoy, K. Liu, R. Nazaryan, X. Lv, P.R. Zangara, B. Safvati, G. Wang, D. Arnold, G. Li, A. Lin, et al., Scien. Advan. 4 (2018).
- [21] Q. Chen, I. Schwarz, F. Jelezko, A. Retzker, M.B. Plenio, Phys. Rev. B 93 (2016), 060408.
- [22] M.D. Lingwood, T.A. Siaw, N. Sailasuta, O.A. Abulseoud, H.R. Chan, B.D. Ross, P. Bhattacharya, S. Han, Radiology 265 (2012) 418–425.
- [23] D. Abrams, M.E. Trusheim, D.R. Eng, M.D. Shattuck, C.A. Meriles, Nano Lett. 14 (2014) 2471–2478.
- [24] Y. Xing, L. Dai, Nanomedicine 4 (2009) 207–218.
- [25] L. Ginés, S. Mandal, D.J. Morgan, R. Lewis, P.R. Davies, P. Borri, G.W. Morley, O.A. Williams, ACS Omega 3 (2018) 16099–16104.
- [26] J.-P. Boudou, P.A. Curmi, F. Jelezko, J. Wrachtrup, P. Aubert, M. Sennour, G. Balasubramanian, R. Reuter, A. Thorel, E. Gaffet, Nanotechnology 20 (2009) 235602.
- [27] V.N. Mochalin, O. Shenderova, D. Ho, Y. Gogotsi, Nat. Nanotechnol. 7 (2012) 11.
- [28] Z.Q. Chu, S. Zhang, B. Zhang, C. Zhang, C.-Y. Fang, I. Rehor, P. Cigler, H.-C. Chang, G. Lin, R. Liu, Q. Li, Sci. Rep. 4 (2014) 4495.
- [29] V. Paget, J.A. Sergeant, R. Grall, S. Altmeyer-Morel, H.A. Girard, T. Petit, C. Gesset, M. Mermoux, P. Bergonzo, J.C. Arnault, S. Chevillard, Nanotoxicology 8 (2014) 46–56. PMID: 24266793.
- [30] Z.-F. Zhang, X.-P. Jia, X.-B. Liu, M.-H. Hu, Y. Li, B.-M. Yan, H.-A. Ma, Chin. Phys. B 21 (2012), 038103.
- [31] V.A. Davydov, A.V. Rakhmanina, S.G. Lyapin, I.D. Ilichev, K.N. Boldyrev, A.A. Shiryayev, V.N. Agafonov, JETP Lett. (Engl. Transl.) 99 (2014) 585–589.
- [32] H. Siampour, S. Kumar, V.A. Davydov, L.F. Kulikova, V.N. Agafonov, S.I. Bozhevolnyi, Light Sci. Appl. 7 (2018) 61.
- [33] S. Choi, V. Leong, V.A. Davydov, V.N. Agafonov, M.W. Cheong, D.A. Kalashnikov, L.A. Krivitsky, Sci. Rep. 8 (2018) 3792.
- [34] G. Dantelle, A. Slablab, L. Rondin, F. Lainé, F. Carrel, P. Bergonzo, S. Perruchas, T. Gacoin, F. Treussart, J.-F. Roch, J. Lumin. 130 (2010) 1655–1658. Special Issue based on the Proceedings of the Tenth International Meeting on Hole Burning, Single Molecule, and Related Spectroscopies: Science and Applications (HBSM 2009) - Issue dedicated to Ivan Lorgere and Oliver Guillot-Noel.
- [35] C. Laube, T. Oeckinghaus, J. Lehnert, J. Griebel, W. Knolle, A. Denisenko, A. Kahnt, J. Meijer, J. Wrachtrup, B. Abel, Nanoscale 11 (2019) 1770–1783.
- [36] M. Capelli, A.H. Heffernan, T. Ohshima, H. Abe, J. Jeske, A. Hope, A.D. Greentree, P. Reineck, B.C. Gibson, Carbon 143 (2019) 714–719.
- [37] B. Slepetz, M. Kertesz, Phys. Chem. Chem. Phys. 16 (2014) 1515–1521.
- [38] B. Slepetz, I. Laszlo, Y. Gogotsi, D. Hyde-Volpe, M. Kertesz, Phys. Chem. Chem. Phys. 12 (2010) 14017–14022.
- [39] F. Fávoro de Oliveira, D. Antonon, Y. Wang, P. Neumann, S. Ali Momenzadeh, T. Häußermann, A. Pasquarelli, A. Denisenko, J. Wrachtrup, Nat. Commun. 8 (2017) 15409.

- [40] W.V. Smith, P.P. Sorokin, I.L. Gelles, G.J. Lasher, *Phys. Rev.* 115 (1959) 1546–1552.
- [41] J.H.N. Loubser, J.A. van Wyk, *Rep. Prog. Phys.* 41 (1978) 1201–1248.
- [42] J.F. Barry, J.M. Schloss, E. Bauch, M.J. Turner, C.A. Hart, L.M. Pham, R.L. Walsworth, *Rev. Mod. Phys.* 92 (1) (2020) 15004.
- [43] A. Raitsimring, K. Salikhov, *Bull. Magn. Reson.* 7 (1985) 184–217.
- [44] S. Agnello, R. Boscaino, M. Cannas, F. Gelardi, *Phys. Rev. B* 64 (2001) 174423.
- [45] M. Brustolon, A. Zoleo, A. Lund, *J. Magn. Reson.* 137 (1999) 389–396.
- [46] A.M. Tyryshkin, S. Tojo, J.J.L. Morton, H. Riemann, N.V. Abrosimov, P. Becker, H.-J. Pohl, T. Schenkel, M.L.W. Thewalt, K.M. Itoh, S.A. Lyon, *Nat. Mater.* 11 (2012) 143–147.
- [47] A. Lund, M. Shiotani, *EPR of Free Radicals in Solids II*, Springer, 2 edition, Springer, Netherlands, 2017.
- [48] K. Salikhov, S. Dzuba, A.M. Raitsimring, *J. Magn. Reson.* 42 (1981) 255–276.
- [49] G.E. Pake, *J. Chem. Phys.* 16 (1948) 327–336.
- [50] E. Wasserman, L.C. Snyder, W.A. Yager, *J. Chem. Phys.* 41 (1964) 1763–1772.
- [51] B.C. Rose, C.D. Weis, A.M. Tyryshkin, T. Schenkel, S.A. Lyon, *Diam. Relat. Mater.* 72 (2018) 32.
- [52] C. Kittel, E. Abrahams, *Phys. Rev.* 90 (1953) 238–239.
- [53] H. Hayashi, T. Itahashi, K.M. Itoh, L.S. Vlasenko, M.P. Vlasenko, *Phys. Rev. B* 80 (2009), 045201.
- [54] G.B. Furman, A.M. Panich, A. Yochelis, E.M. Kunoff, S.D. Goren, *Phys. Rev. B* 55 (1997) 439–444.
- [55] A.M. Panich, N.A. Sergeev, A.I. Shames, V.Y. Osipov, J.-P. Boudou, S.D. Goren, *J. Phys. Condens. Matter* 27 (2015), 072203.
- [56] W.E. Blumberg, *Phys. Rev.* 119 (1960) 79–84.
- [57] N. Benetis, J. Kowalewski, L. Nordenskiöld, H. Wennerström, P.-O. Westlund, *Mol. Phys.* 48 (1983) 329–346.
- [58] C. Bradac, T. Gaebel, N. Naidoo, J.R. Rabeau, A.S. Barnard, *Nano Lett.* 9 (2009) 3555–3564. PMID: 19705805.
- [59] S. Felton, A.M. Edmonds, M.E. Newton, P.M. Martineau, D. Fisher, D.J. Twitchen, J.M. Baker, *Phys. Rev. B* 79 (2009), 075203.
- [60] E.C. Reynhardt, G.L. High, *J. Chem. Phys.* 109 (1998) 4090–4099.
- [61] Z.J. Wang, M.A. Ohliger, P.E.Z. Larson, J.W. Gordon, R.A. Bok, J. Slater, J.E. Villanueva-Meyer, C.P. Hess, J. Kurhanewicz, D.B. Vigneron, *Radiology* (2019) 182391, 0.
- [62] T. Boele, D.E.J. Waddington, T. Gaebel, E. Rej, A. Hasija, L.J. Brown, D.R. McCamey, D.J. Reilly, *Phys. Rev. B* 101 (15) (2020) 155416.
- [63] V. Davydov, A. Rakhmanina, V. Agafonov, B. Narymbetov, J.-P. Boudou, H. Szwarc, *Carbon* 42 (2004) 261–269.
- [64] V. Davydov, A. Rakhmanina, V. Agafonov, V. Khabashesku, *Carbon* 90 (2015) 231.
- [65] S. Stoll, A. Schweiger, *J. Magn. Reson.* 178 (2006) 42–55.